Electronic Supporting Information File: Unveiling the Interaction Between Fragments of ABX_3 Halide Perovskite and $Ti_3C_2F_2$ MXene Monolayer

Paulo E. Zanni Jr.,[†] Lucas G. Chagas,[†] Rafael L. H. Freire,[‡] Juarez L. F. Da Silva,[‡] and Matheus P. Lima[*,†]

†*Department of Physics, Federal University of São Carlos*, 13565-905, *São Carlos, SP, Brazil*

‡*São Carlos Institute of Chemistry, University of São Paulo, Av. Trabalhador São-Carlense 400*, 13560-970, *São Carlos, SP, Brazil*

E-mail: mplima@df.ufscar.br

Contents

S-1 INTRODUCTION

The motivation for investigating the interaction between fragments of organometal trihalide perovskites[1,2] (ABX_3) and two-dimensional materials such as MXenes[3,4] ($M_{n+1}X_nT_x$) in the context of solar cells stems from the need to explore material interactions to advance energy-related technologies, as interfaces are inevitable. Specifically, the number of works using MXenes in perovskite solar cells has recently grown. On the social front, improved materials could improve the efficiency of renewable energy devices, such as solar cells, making clean energy more accessible and affordable to communities. Economically, advances in energy technology often lead to the growth of new industries[5] and employment opportunities. Thus, the study findings have the potential to drive positive changes both socially and economically.

S-2 ADDITIONAL COMPUTATIONAL DETAILS

Table S-1. Technical details of the selected PAW projectors for each specie in this study. All files were obtained from the potpaw_PBE_5.4_2020_01_15 library. The table presents the most important information of the selected projectors, which includes the atomic species (Element) ordered by atomic number, the name of the projectors (TITEL), date of projector creation (Date), number of valence electrons (Z_{val}), valence electronic configuration (Valence), the minimum (`ENMIN`) and the maximum (`ENMAX`) recommended cutoff energies in units of eV for the plane-wave basis set for each element.

Element	TITEL	Date	Z_{val}	Valence	`ENMIN`	`ENMAX`
Pb	Pb_d_GW	14/04/2014	16	$5s^2 5d^{10} 6s^2 2p^2$	178.357	237.809
Cs	Cs_sv_GW	23/03/2010	9	$5s^2 5p^6 5d^1$	148.575	198.101
I	I_GW	12/03/2012	7	$5s^2 5p^5$	131.735	175.647
Br	Br_GW	20/03/2012	7	$4s^2 4p^5$	162.214	216.285
Ti	Ti_sv_GW	05/12/2013	12	$3s^2 3p^6 3d^4$	287.830	383.774
Cl	Cl_GW	19/03/2012	7	$3s^2 3p^5$	196.854	262.472
F	F_GW_new	19/03/2012	7	$2s^2 2p^5$	365.773	487.698
N	N_GW_new	19/03/2012	5	$2s^2 2p^3$	315.677	420.902
C	C_GW_new	19/03/2012	4	$2s^2 2p^2$	310.494	413.992
H	H_GW	21/04/2008	1	$1s^1$	250.000	300.000

S-3 COMPUTATIONAL CONVERGENCE TESTS

S-3.1 The Role of the Number of k-points and Cutoff Energies

We conducted convergence tests for **k**-points and cutoff energy for the $Ti_3C_2F_2$ MXene. We optimized the unit cell using stress tensor calculations, freezing the lattice vector in the direction perpendicular to the monolayer plane. For the **k**-points convergence tests, we used a cutoff energy of 2×ENMAX$_{max}$ = 975.396 eV (see Table S-1), and increased the N×N×1 **k**-points from 4×4×1 to 40×40×1, with variations in N by increments of 4. For the cutoff energy convergence tests, we used a 12×12×1 **k**-points, and increased the m×ENMAX$_{max}$ cutoff energy from 1.125 to 2.250, with variations in m by increments of 0.125. Figure S-1 shows the properties calculated.

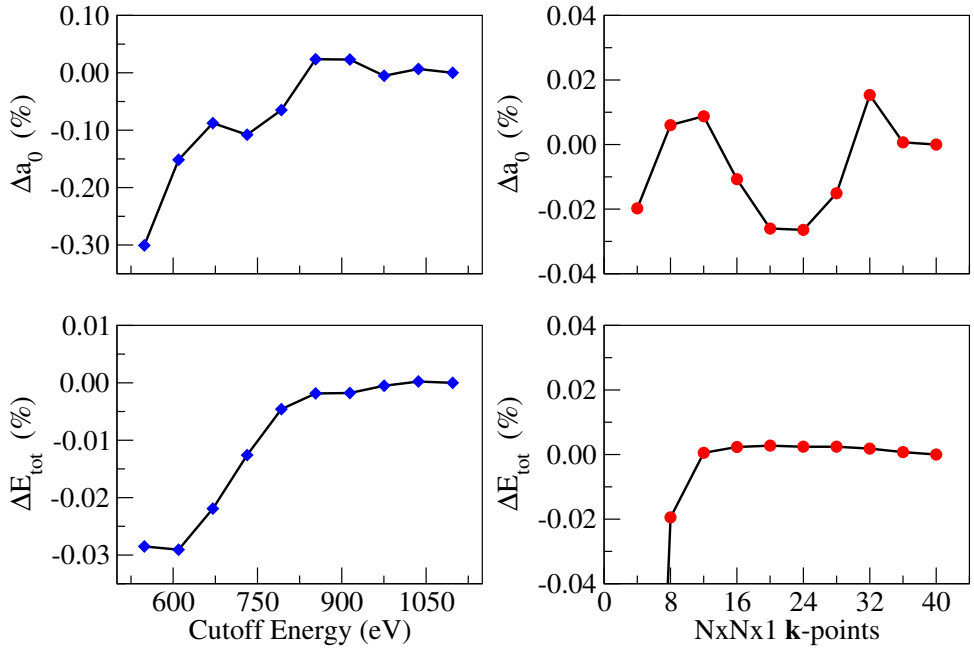

Figure S-1. The convergence of the relative total energy (ΔE_{tot}) and the relative lattice parameter (Δa_0) of the unit cell as functions of cutoff energy (blue diamonds) and **k**-points (red dots). The relative total energy (ΔE_{tot}) is defined using the following equation: $\Delta E_{tot} = E_{tot} - E_{tot}^{ref}$. The relative lattice parameter (Δa_0) is defined using the following equation: $\Delta a_0 = a_0 - a_0^{ref}$. Here, we select the 2.250×ENMAX$_{max}$ cutoff energy configuration as the reference and the 40×40×1 **k**-points configuration as the reference.

Based on these calculations, we conclude that a cutoff energy value of 2×ENMAXmax = 975.396 eV along with a **k**-point mesh of 12×12×1 will be suitable to achieve the asymptotic behavior of properties calculated with stress tensor calculations. Meanwhile,

a value of 1.125×ENMAXmax = 548.660 eV is suitable for calculations employing a frozen structure.

S-3.2 Comparison Between 1×1×1 k-points and 4×4×1 k-points in the 3×3 Supercell

Following the 1×1 unit cell optimization, a 3×3 supercell is constructed to carry out convergence tests, encompassing the primary properties (structural, energetic, and electronic) expected to be evaluated in this study. These tests aim to compare both the 1×1×1 **k**-points (Γ-point) and the 4×4×1 **k**-points. To calculate the relevant properties, we adsorbed the Br^- atom at the four sites commonly used for MXenes, as reported in the literature and shown in the main text. The Br^- atom was chosen because it has a medium atomic radius compared to the other possibilities for X^- (i.e., $X^- = Cl^-$, Br^-, and I^-) in ABX_3 perovskites. For all adsorbed cases, we generated structures to ensure point-inversion symmetry by adsorbing atoms and molecules symmetrically on both sides of the slab, thus avoiding the formation of superficial dipoles.

After optimization through stress tensor calculations, we analyzed the structural parameters to compare the 1×1×1 **k**-points and the 4×4×1 **k**-points. Table S-2 shows the distances after relaxation between the adsorbed Br^- atom and the slab, as well as between the adsorbed Br^- atom and the atom below. The data indicate a negligible influence on the relaxed distances due to both the 1×1×1 **k**-points and the 4×4×1 **k**-points. Additionally, we emphasize that the Br^- atom adsorbed at the Bridge site migrates to the Top Ti site after relaxation.

Table S-2. Distances between the adsorbed Br^- atom and the slab ($d_{Br-Slab}$), as well as between the adsorbed Br^- atom and the atom below ($d_{Br-Atom}$), after structural optimizations. Here, the geometry optimizations were performed for distinct adsorption sites using both the 1×1×1 as well as the 4×4×1 **k**-point samplings for the Brillouin zone.

Site	$d^{1\times1\times1}_{Br-Slab}$ (Å)	$d^{1\times1\times1}_{Br-Atom}$ (Å)	$d^{4\times4\times1}_{Br-Slab}$ (Å)	$d^{4\times4\times1}_{Br-Atom}$ (Å)
Top F	2.79	2.84 (Br–F)	2.79	2.84 (Br–F)
Top Ti	1.68	2.64 (Br–Ti)	1.62	2.60 (Br–Ti)
Hollow	2.54	4.83 (Br–C)	2.56	4.86 (Br–C)
Bridge	1.68	2.63 (Br–Ti)	1.65	2.62 (Br–Ti)

In Figure S-2, we show the distances in pristine MXene after geometry optimization. We found that the Ti−F distance changes by approximately 0.004 Å, and the C−Ti distance changes by 0.006 Å when comparing the 1×1×1 and 4×4×1 **k**-points. The data in Table S-2 and Figure S-2 indicate that since these changes are small compared to the available experimental precision, it is prudent to perform preliminary relaxations only at the 1×1×1 **k**-points to obtain relaxed geometries. This procedure saves computational time while maintaining numerical accuracy and precision.

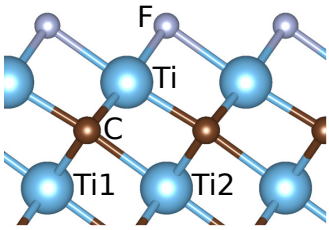

Distances in (Å) for **k-points** and	**1x1x1 k-points**	**4x4x1 k-points**
Ti—F	2.1609	2.1642
C—Ti	2.0665	2.0623
C—Ti1	2.1851	2.1794
C—Ti2	3.7556	3.7523

Figure S-2. Comparison among distances in the geometry of the 3×3 supercell for pristine $Ti_3C_2F_2$ MXene after relaxation using both 1×1×1 **k**-points and 4×4×1 **k**-points.

Regarding the energetic properties, Table S-3 presents the total energy, the relative total energy, and the adsorption energy. The lowest energy system occurs when the Br^- atom is adsorbed at the bridge site and migrates to the Top Ti site after relaxation. In terms of energy, unlike distances, we observe that the **k**-points are relevant. There is an approximate 2.00 eV difference in total energy between the 1×1×1 **k**-points and the 4×4×1 **k**-points, as well as a 0.50 eV difference in adsorption energy for the lowest-energy system when comparing both meshes.

Table S-3. The total energy (E_{tot}), relative total energy (ΔE_{tot}), and adsorption energy (E_{ad}) of adsorption sites at the 1×1×1 **k**-points and at the particular 4×4×1 **k**-points. The relative total energy (ΔE_{tot}) is defined using the following equation: $\Delta E_{tot} = E_{tot} - E_{tot}^{ref}$. Here, we select the lowest energy configuration as the reference. The adsorption energy (E_{ad}) is defined as follows: $E_{ad} = E_{tot}^{Ti_3C_2F_2/Br(111)} - E_{tot}^{Ti_3C_2F_2} - E_{tot}^{Br(111)}$.

Site	$E_{tot}^{1\times1\times1}$ (eV)	$\Delta E_{tot}^{1\times1\times1}$ (eV)	$E_{ad}^{1\times1\times1}$ (eV)	$E_{tot}^{4\times4\times1}$ (eV)	$\Delta E_{tot}^{4\times4\times1}$ (eV)	$E_{ad}^{4\times4\times1}$ (eV)
Top F	−601.18	1.24	−1.46	−599.33	0.91	−1.29
Top Ti	−602.39	0.02	−2.67	−600.24	0.01	−2.19
Hollow	−601.38	1.04	−1.66	−599.48	0.77	−1.43
Bridge	−602.41	0.00	−2.70	−600.25	0.00	−2.20

Once we verified in Table S-3 that the **k**-points are relevant for energy calculations, we performed an additional test by calculating the adsorption energy using the optimized geometry at the 1×1×1 **k**-points but with the 4×4×1 **k**-points added. These calculations were performed in one step with the atoms kept static, and the results are shown in Table S-4. We can observe that there are no significant differences between $E_{ad}^{\Gamma\rightarrow\mathbf{k}}$ and $E_{ad}^{4\times4\times1}$. This indicates that the geometries with adsorbed fragments can be optimized using only the 1×1×1 grid, after which a denser **k**-point sampling can be used to calculate these properties with the frozen structure. Therefore, we can calculate energies with 4×4×1 **k**-points in one step rather than perform a full relaxation.

Table S-4. The adsorption energy ($E_{ad}^{\Gamma\rightarrow\mathbf{k}}$) is calculated using the static geometry resulting from relaxation with 1×1×1 **k**-points, but increasing to 4×4×1 **k**-points for a single-step ionic calculation.

Site	$E_{ad}^{1\times1\times1}$ (eV)	$E_{ad}^{\Gamma\rightarrow\mathbf{k}}$ (eV)	$E_{ad}^{4\times4\times1}$ (eV)
Top F	−1.46	−1.32	−1.29
Top Ti	−2.67	−2.19	−2.19
Hollow	−1.66	−1.43	−1.43
Bridge	−2.70	−2.20	−2.20

S-3.3 Supercell Size Investigation

To determine the influence of supercell size, we adsorbed a Br^- atom at the Top Ti site (the lowest energy site) and calculated the adsorption energy for 3×3, 4×4, and 5×5 supercells using 4×4×1, 3×3×1, and 2×2×1 **k**-points, respectively. The adsorption energy ($E_{ad}^{\Gamma\rightarrow\mathbf{k}}$) is calculated using the static geometry resulting from relaxation with 1×1×1 **k**-points, but increasing **k**-points for a single-step ionic calculation. We found that the size of the supercell does not significantly affect the adsorption energy when **k**-points are added. Therefore, we only need to ensure that the adsorbed molecule is far enough, at least 8.00 Å, from its periodic image when choosing the supercell size.

Table S-5. Tests with different supercell sizes and different k-meshes

Supercell	$d_{\mathrm{Br-Ti}}^{1\times1\times1}$ (Å)	$E_{ad}^{1\times1\times1}$ (eV)	$E_{ad}^{\Gamma\rightarrow\mathbf{k}}$ (eV)
3×3	2.63	−2.70	−2.20
4×4	2.61	−3.02	−2.19
5×5	2.54	−2.36	−2.20

S-4 ADDITIONAL RESULTS FOR PRISTINE $Ti_3C_2F_2$ MONOLAYER

S-4.1 Structure Models

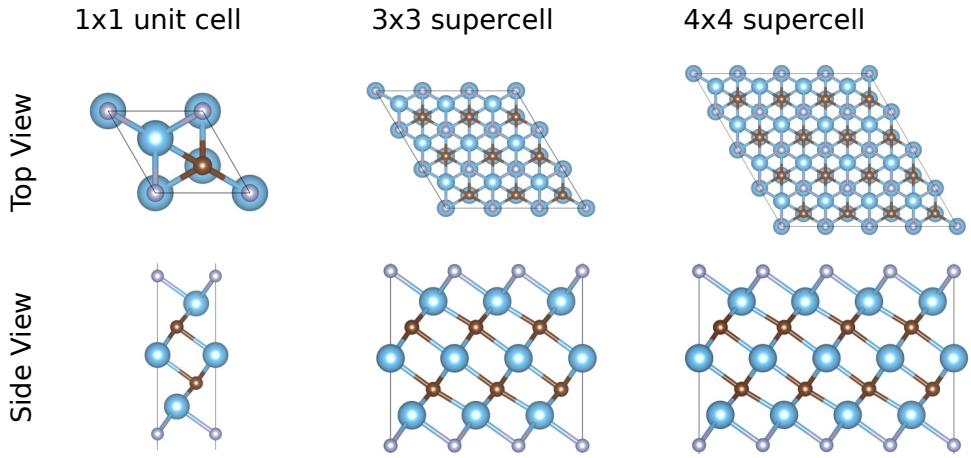

Figure S-3. Optimized structures for $Ti_3C_2F_2$ MXene highlighting the top view and side view of the 1×1 unit cell, 3×3 supercell, and 4×4 supercell.

S-4.2 Geometric Parameters

We obtained the 1×1 unit cell lattice parameter using stress-tensor calculations, and the supercells were constructed with this 1×1 unit cell lattice parameter. We obtained a calculated lattice parameter for the $Ti_3C_2F_2$ MXene monolayer of $a_0 = 3.054$ Å. Table S-6 summarizes the lattice parameters found in theoretical studies in the literature. Therefore, we conclude that our calculated lattice parameters are in agreement with the theoretical results.

Table S-6. Literature review – quantum chemistry code (QC Code), exchange-correlation energy fuctional (XC), lattice parameter (a_0) in Å, and Reference number (Ref.) for the $Ti_3C_2F_2$ MXene monolayer.

QC Code	XC	a_0	Ref.
VASP	GGA-PBE	3.054	This work
CASTEP	GGA-WC[6]	3.019	7
VASP	GGA-PBE	3.079	8
VASP	GGA-PBE	3.077	9
VASP	GGA-HSE06[10]	3.051	9
CASTEP	GGA-PBE	3.076	11
QE	GGA-PBE	3.060	12

S-4.3 Energetic Properties

Table S-7. Total energies (E_{tot}^{slab}) were calculated for pristine $Ti_3C_2F_2$ MXene using the 1×1 unit cell and the 3×3, 4×4, and 5×5 supercells. For the 1×1 unit cell, we obtained the total energy using the stress-tensor method with 12×12×1 **k**-points. For the supercells, we performed the stress-tensor calculations using 1×1×1 **k**-points (relaxations using Γ-point only) and then added the **k**-points to obtain the total energies in a single-step ionic calculation.

Cell Size	E_{tot}^{slab} (eV/f.u.)	**k**-mesh
1×1	−66.41	12×12×1
3×3	−66.39	4×4×1
4×4	−66.39	3×3×1
5×5	−66.39	2×2×1

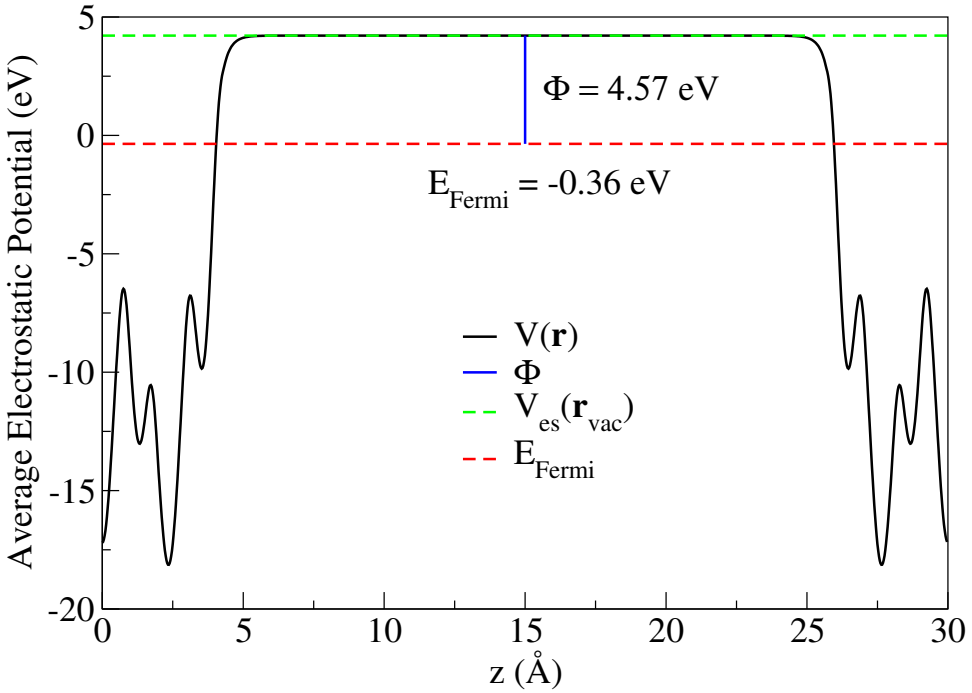

Figure S-4. The work function (Φ) calculated for the 1×1 unit cell, defined as the energy difference between the electrostatic potential at the vacuum level ($V_{es}(\mathbf{r}_{vac})$) and the highest occupied state within the band structure (E_{Fermi}), i.e., $\Phi = V_{es}(\mathbf{r}_{vac}) - E_{\text{Fermi}}$.

S-5 ADDITIONAL RESULTS ON PEROVSKITE FRAGMENTS IN THE GAS PHASE

S-5.1 Selected Chemical Species and Structure Models

This work explores fragments of ABX_3 organometal trihalide perovskites, including A^+, B^{2+}, X^-, AX, BX_2 adsorbed on MXenes. For the organic cation A^+, we will use three elements: the Methylammonium (MA^+) $CH_3NH_3{}^+$ molecule, the Formamidinium (FA^+) $HC(NH_2)_2{}^+$ molecule, and the Cesium (Cs^+) atom. For the metal cation B^{2+}, we will use only one element: Lead (Pb^{2+}) atom. For the halide anion X^-, we will use three elements: the Chlorine (Cl^-), the Bromine (Br^-), and the Iodine (I^-) atomic species. Figure S-5 presents the MA^+ and FA^+ molecules. For AX and BX_2, we will explore all combinations of elements mentioned for A^+, B^{2+}, and X^-.

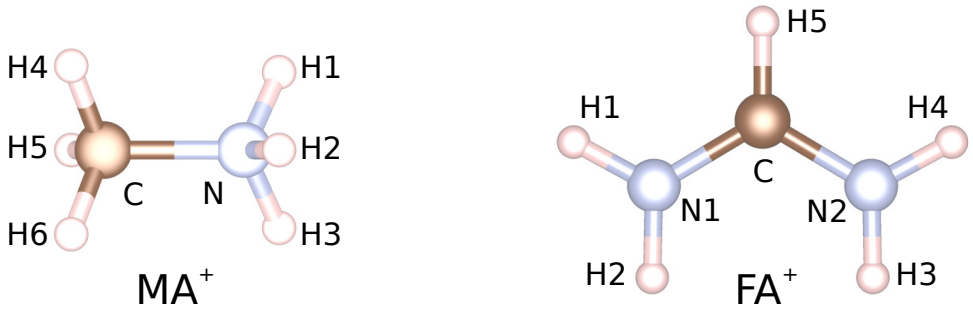

Figure S-5. Relaxed structures in the gas phase of the molecular ions: Methylammonium (left) and Formamidinium (right). Tables S-8 and S-9 present the distances and a comparison with the literature.

Table S-8. Internal bond length distances of the molecular ion MA^+, namely the distances between H and C atoms (H−C), C and N atoms (C−N), and N and H atoms (N−H). Here, the distances between N and its nearest hydrogen atoms (H_1, H_2, and H_3) are equal. Similarly, the distances between C and its nearest hydrogen atoms (H_4, H_5, and H_6) are equal.

Molecule	Distances (Å)			Ref.
	H−C	C−N	N−H	
MA^+	1.094	1.509	1.031	This work
	1.060	1.467	1.030	13

Table S-9. Internal bond length distances of the molecular ion FA^+, namely the distances between H and C atoms (H−C), C and N atoms (C−N), and N and H atoms (N−H). Here, the distances between C and the nitrogen atoms (N_1, N_2) are equal. The distance between N_1 and H_1 is equal to the distance between N_2 and H_4, and the distance between N_1 and H_2 is equal to the distance between N_2 and H_3.

Molecule	Distances (Å)				Ref.
	H_5−C	C−N	N_1−H_1	N_2−H_3	
FA^+	1.081	1.393	1.007	1.009	This work
	1.089	1.298	1.012	1.022	13

To model MACl, MABr, MAI, FACl, FABr, and FAI molecules, we first considered the MA fragment and placed the Br halogen atom in different positions. The initial and optimized geometries of the MABr molecule are shown in Figure S-6. This procedure was carried out in the gas phase for all molecules to identify the lowest-energy configuration.

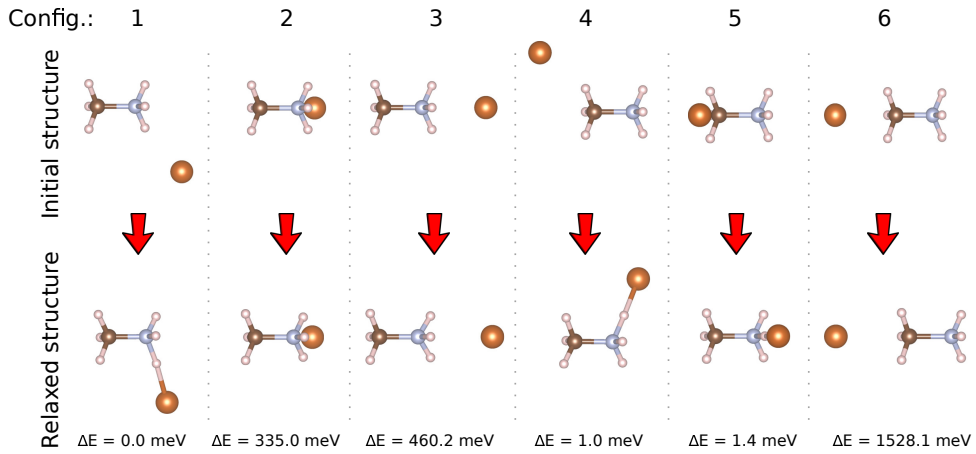

Figure S-6. MABr molecules in the gas phase. The upper panels show the initial geometries, and the bottom panels show the optimized geometries. This procedure was carried out to find the lowest energy configuration. We performed this procedure for MACl, MABr, MAI, and FABr molecules.

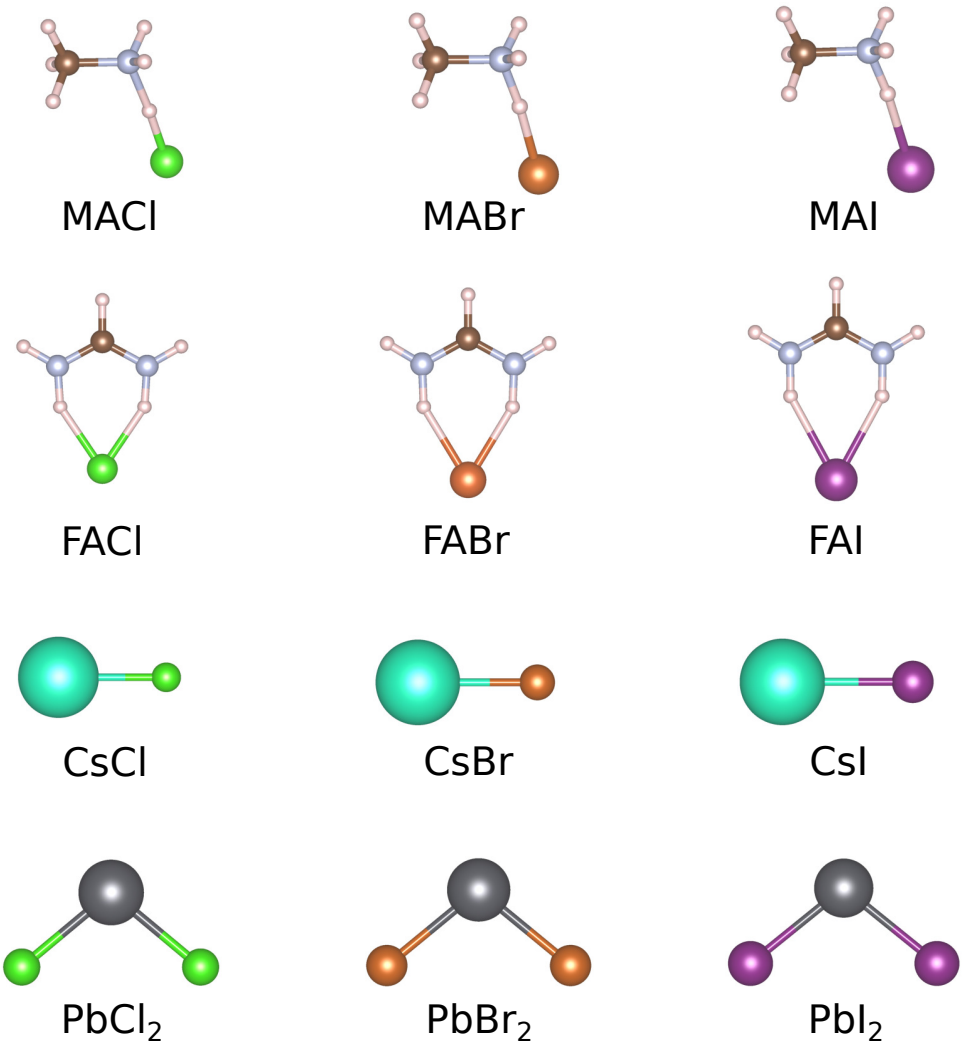

Figure S-7. All relaxed structures of molecules that will be adsorbed on the surface of $Ti_3C_2F_2$ MXene. Tables S-10, S-11, and S-12 show the interatomic distances of these molecules. For CsX the distances are 2.904, 3.073, 3.323 for X = Cl, Br, I, respectively.

Table S-10. Interatomic distances of *MAX* molecules.

Molecule	Distances (Å)							
	H_4-C	H_5-C	H_6-C	$C-N$	$N-H_1$	$N-H_2$	$N-H_3$	H_3-X
MACl	1.100	1.097	1.097	1.474	1.022	1.022	1.437	1.454
MABr	1.097	1.096	1.096	1.480	1.023	1.024	1.253	1.743
MAI	1.096	1.095	1.095	1.483	1.024	1.024	1.188	2.025

Table S-11. Interatomic distances of *FAX* molecules.

Molecule	Distances (Å)				
	H_5-C	$C-N$	N_1-H_1	N_2-H_3	H_3-X
FACl	1.903	1.317	1.012	1.076	1.960
FABr	1.903	1.317	1.013	1.070	2.134
FAI	1.903	1.317	1.013	1.063	2.379

Table S-12. Interatomic distances of PbX_2 triatomic molecules with their respective angles.

Molecule	Distances (Å)		Angles (°)
	$Pb-X$	$X-X$	
$PbCl_2$	2.486	3.822	100.48
$PbBr_2$	2.630	4.062	101.10
PbI_2	2.835	4.405	101.95

S-5.2 Energetic and Eletronic Properties

Table S-13. The highest occupied molecular orbital (HOMO), illustrating the absence of fractional orbitals, total energy (E_{tot}), binding energy (E_b) in the AX and BX_2 molecules, and the *spin* (**S**) were calculated as the difference between the number of up and down electrons of perovskite fragments calculated in the gas phase. Calculations were done with box dimensions of 25.0 Å×26.0 Å×27.0 Å and `ENCUT` = 548.660 eV.

Formula	HOMO	E_{tot}^{gas} (eV)	E_b (eV)	**S** ($\frac{\hbar}{2}$)
MA^+	1.00	−37.20	-	1.00
FA^+	1.00	−42.21	-	1.00
Cs^+	1.00	−1.81	-	1.00
Pb^{2+}	1.00	−0.62	-	2.00
Cl^-	1.00	−0.24	-	1.00
Br^-	1.00	−0.27	-	1.00
I^-	1.00	−0.21	-	1.00
MACl	1.00	−42.39	−4.96	0.00
MABr	1.00	−41.78	−4.31	0.00
MAI	1.00	−41.17	−3.76	0.00
FACl	1.00	−47.22	−4.77	0.00
FABr	1.00	−46.68	−4.20	0.00
FAI	1.00	−46.10	−3.68	0.00
CsCl	1.00	−6.65	−4.60	0.00
CsBr	1.00	−6.16	−4.09	0.00
CsI	1.00	−5.63	−3.61	0.00
$PbCl_2$	1.00	−9.42	−8.32	0.00
$PbBr_2$	1.00	−8.45	−7.30	0.00
PbI_2	1.00	−7.41	−6.37	0.00

S-6 ADDITIONAL RESULTS ON PEROVSKITE FRAGMENTS ON $Ti_3C_2F_2$ MXENE

S-6.1 Geometric Parameters

Table S-14. All 216 systems were initially adsorbed at a vertical distance of 2.5 Å from the slab. This table shows the vertical distances (h) of the adsorbed systems on the slab after structural relaxation, with the **bold** values indicating the configurations with the lowest energy and the remaining values corresponding to higher energy systems.

Formula	Configuration	Vertical Distance (Å)			
		Top F	Top Ti	Hollow	Bridge
MA^+	1	1.470	1.459	1.459	**1.433**
	2	1.907	1.587	1.557	1.495
	3	2.215	2.089	2.227	1.447
FA^+	1	1.604	1.910	1.975	1.983
	2	1.478	**1.534**	1.557	1.545
	3	1.564	1.549	1.991	1.549
	4	1.588	1.632	1.431	1.300
Cs^+	-	2.580	**2.318**	2.310	2.314
Pb^{2+}	-	**2.419**	1.939	2.441	1.952
Cl^-	-	2.615	**1.390**	0.172	1.399
Br^-	-	2.765	1.653	2.381	**1.649**
I^-	-	2.997	2.020	**2.758**	2.015
MACl	1	1.919	1.828	**1.846**	1.817
	2	2.318	1.971	1.988	1.845
	3	2.351	2.042	2.087	2.041

Continued on next page

Table S-14 Continued from previous page

Formula	Configuration	Vertical Distance (Å)			
		Top F	Top Ti	Hollow	Bridge
MABr	1	1.879	1.764	**1.809**	1.760
	2	1.717	1.932	1.939	1.796
	3	2.323	2.075	2.112	2.131
MAI	1	1.777	1.720	**1.775**	1.738
	2	1.715	1.876	1.860	1.755
	3	2.305	2.094	2.009	2.028
FACl	1	2.173	2.435	1.661	1.984
	2	3.001	2.666	2.671	2.603
	3	2.560	2.663	**2.399**	2.610
	4	1.844	1.818	1.814	1.872
FABr	1	2.167	1.865	1.757	2.130
	2	3.035	2.742	2.765	2.476
	3	2.516	2.577	**2.345**	2.577
	4	1.952	1.792	1.820	1.824
FAI	1	2.025	1.711	1.595	1.858
	2	3.182	3.009	3.011	2.437
	3	2.452	2.459	**2.270**	2.513
	4	1.789	1.759	1.788	1.795
CsCl	1	**2.596**	2.654	2.581	2.653
	2	3.019	2.665	2.700	2.592
	3	3.097	2.797	2.843	2.827

Continued on next page

Table S-14 Continued from previous page

Formula	Configuration	Vertical Distance (Å)			
		Top F	Top Ti	Hollow	Bridge
CsBr	1	2.793	2.800	**2.734**	2.765
	2	3.017	2.742	2.800	2.790
	3	3.060	2.768	2.705	2.779
CsI	1	2.790	2.777	2.720	**2.772**
	2	3.013	2.730	2.762	2.792
	3	3.231	3.023	3.036	2.973
$PbCl_2$	1	2.909	2.613	2.595	2.551
	2	2.635	2.877	2.707	2.743
	3	2.711	2.507	2.695	**2.718**
	4	2.873	2.817	2.837	2.900
$PbBr_2$	1	2.648	2.672	2.721	2.773
	2	2.938	2.734	2.716	2.917
	3	**2.734**	2.712	2.715	2.744
	4	3.052	2.854	2.834	2.957
PbI_2	1	2.964	2.713	2.697	2.767
	2	3.172	2.747	2.764	3.113
	3	2.711	2.749	2.742	**2.699**
	4	2.853	3.113	2.582	3.080

S-6.2 Site Preference

Table S-15. We present the specific sites along with their corresponding configurations that led the adsorbed system to the lowest energy (i.e., the configurations in bold in Table S-14) after adsorption optimization.

Type	Formula	Site Preference	Configuration
A^+	MA^+	Bridge	1
	FA^+	Top Ti	2
	Cs^+	Top Ti	-
B^{2+}	Pb^{2+}	Top F	-
X^-	Cl^-	Top Ti	-
	Br^-	Bridge	-
	I^-	Hollow	-
AX	MACl	Hollow	1
	MABr	Hollow	1
	MAI	Hollow	1
	FACl	Hollow	3
	FABr	Hollow	3
	FAI	Hollow	3
	CsCl	Top F	1
	CsBr	Hollow	1
	CsI	Bridge	1
BX_2	$PbCl_2$	Bridge	3
	$PbBr_2$	Top F	3
	PbI_2	Bridge	3

S-6.3 Adsorption Energies, Interaction Energies, and Work Functions

In Table S-16, we present the adsorption energies (E_{ad}), interaction energies (E_{int}), and work functions (Φ) after structural relaxation. For the adsorption energies (E_{ad}), we used $E_{tot}^{slab} = -1062.23\,\text{eV}$ as the total energy of the pristine slab, which corresponds to the energy of the slab in its relaxed phase without any adsorbates; see Ref. S-7. The energies of the gas-phase adsorbates are provided in Ref. S-13, representing their total energies in the isolated and fully relaxed phases. The formula used to calculate E_{ad} was $E_{ad} = \frac{E_{tot}^{system} - E_{tot}^{slab} - 2\times E_{tot}^{gas}}{2}$, where the factors $2\times$ and $\frac{1}{2}$ account for the adsorption on both sides of the slab, following the technique known as point-inversion symmetry. The formula used to calculate E_{int} was $E_{int} = \frac{E_{tot}^{sys} - E_{tot}^{subfrozen} - E_{tot}^{gasfrozen}}{2}$, where the factor $\frac{1}{2}$ accounts for adsorption on both sides of the slab, following the technique known as

point-inversion symmetry, and for E_{int} does not have the factor 2×, once the energy of both frozen molecules was calculated together. For the work functions (Φ), we use the formula given by $\Phi = V_{es}(\mathbf{r}_{vac}) - E_{\text{Fermi}}$, where $V_{es}(\mathbf{r}_{vac})$ is the vacuum energy level and E_{Fermi} is the Fermi energy level.

Table S-16. The adsorption energies (E_{ad}) and the work functions (Φ) for the lowest energy configurations of all optimized structures (i.e., the configurations in bold in Table S-14).

Type	Formula	E_{tot}^{system} (eV)	E_{ad} (eV)	E_{int} (eV)	Φ (eV)
Pristine	-	−1062.23	-	-	4.57
A^+	MA^+	−1140.93	−2.15	−2.51	2.51
	FA^+	−1150.68	−2.02	−2.45	2.50
	Cs^+	−1070.51	−2.34	−2.63	2.21
B^{2+}	Pb^{2+}	−1064.85	−0.69	−0.81	3.65
X^-	Cl^-	−1066.30	−1.80	−3.40	5.27
	Br^-	−1065.04	−1.14	−2.68	5.35
	I^-	−1063.85	−0.60	−0.74	5.92
AX	MACl	−1048.03	−0.51	−0.56	4.52
	MABr	−1147.00	−0.61	−0.63	4.58
	MAI	−1145.96	−0.69	−0.69	4.71
	FACl	−1157.90	−0.62	−0.62	4.66
	FABr	−1156.92	−0.67	−0.65	4.71
	FAI	−1155.86	−0.72	−0.69	4.84
	CsCl	−1077.08	−0.78	−0.80	4.33
	CsBr	−1076.20	−0.83	−0.82	4.44
	CsI	−1075.26	−0.89	−0.84	4.56
BX_2	$PbCl_2$	−1082.42	−0.68	−0.71	4.91
	$PbBr_2$	−1080.54	−0.70	−0.74	4.49
	PbI_2	−1078.56	−0.76	−0.79	4.96

To quantitatively assess the role of long-range van der Waals interactions in the adsorption process, we explicitly isolated the contribution of the D3 dispersion correction from the total DFT+D3 interaction energies. All dispersion terms were evaluated using identical atomic geometries and electronic charge densities, ensuring that the dispersion contribution is treated as a purely additive energetic component. The net dispersion contribution to adsorption, ΔE_{disp}, is defined as $\Delta E_{\text{disp}} = E_{\text{disp}}^{\text{sys}} - E_{\text{disp}}^{\text{sub}} - E_{\text{disp}}^{\text{gas}}$, where $E_{\text{disp}}^{\text{sys}}$ is the dispersion energy of the fully adsorbed system, $E_{\text{disp}}^{\text{sub}}$ corresponds to the clean

MXene substrate, and $E_{\mathrm{disp}}^{\mathrm{gas}}$ denotes the isolated adsorbate in the gas phase. To further quantify the relative importance of dispersion effects in the interaction energy, we define the dimensionless dispersion contribution factor η_{disp} as $\eta_{\mathrm{disp}} = \frac{|\Delta E_{\mathrm{disp}}|}{|E_{\mathrm{int}}|} \times 100\%$, where E_{int} is the total interaction energy obtained from DFT+D3 calculations. This metric directly measures the fraction of the interaction energy arising from dispersion forces. Table S-17 reports the individual dispersion energy components, the resulting ΔE_{disp}, and the corresponding η_{disp} values for all investigated adsorbates. The data reveal that strongly bound ionic species are characterized by relatively small dispersion contributions, while weakly interacting neutral fragments exhibit a dispersion-dominated interaction regime, consistent with their physisorbed nature on the MXene surface.

Table S-17. Dispersion energy contributions to E_{int} for all optimized systems. Strongly bound ionic adsorbates exhibit a limited dispersion contribution, whereas weakly interacting neutral fragments are dominated by van der Waals interactions; the relative impact of dispersion on E_{int} is quantified by η_{disp} for all species adsorbed on the MXene surface.

Type	Formula	$E_{\mathrm{disp}}^{\mathrm{sys}}$ (eV)	$E_{\mathrm{disp}}^{\mathrm{sub}}$ (eV)	$E_{\mathrm{disp}}^{\mathrm{gas}}$ (eV)	ΔE_{disp} (eV)	η_{disp} (%)
A^+	MA^+	−21.0186	−20.1773	−0.0521	−0.79	15.74
	FA^+	−21.1690	−20.1783	−0.0620	−0.93	19.00
	Cs^+	−21.1084	−20.1818	−0.0214	−0.91	17.24
B^{2+}	Pb^{2+}	−21.0342	−20.1784	−0.0014	−0.85	52.61
X^-	Cl^-	−20.5972	−20.1298	−0.0002	−0.47	6.87
	Br^-	−20.7020	−20.1360	−0.0004	−0.57	10.54
	I^-	−20.6747	−20.1711	−0.0006	−0.50	33.92
AX	MACl	−21.1746	−20.1687	−0.1269	−0.88	79.28
	MABr	−21.2722	−20.1686	−0.1376	−0.97	77.14
	MAI	−21.3697	−20.1683	−0.1445	−1.06	76.88
	FACl	−21.4060	−20.1808	−0.1343	−1.09	88.85
	FABr	−21.4967	−20.1817	−0.1472	−1.17	89.79
	FAI	−21.5710	−20.1808	−0.1583	−1.23	89.70
	CsCl	−21.3240	−20.1735	−0.0199	−1.13	71.27
	CsBr	−21.4016	−20.1746	−0.0266	−1.20	73.41
	CsI	−21.4592	−20.1731	−0.0260	−1.26	75.47
BX_2	$PbCl_2$	−21.4226	−20.1707	−0.0324	−1.22	85.78
	$PbBr_2$	−21.5596	−20.1732	−0.0479	−1.34	91.06
	PbI_2	−21.7571	−20.1753	−0.0670	−1.51	96.30

S-6.4 Density of States, Band Structures, and Bader Charges

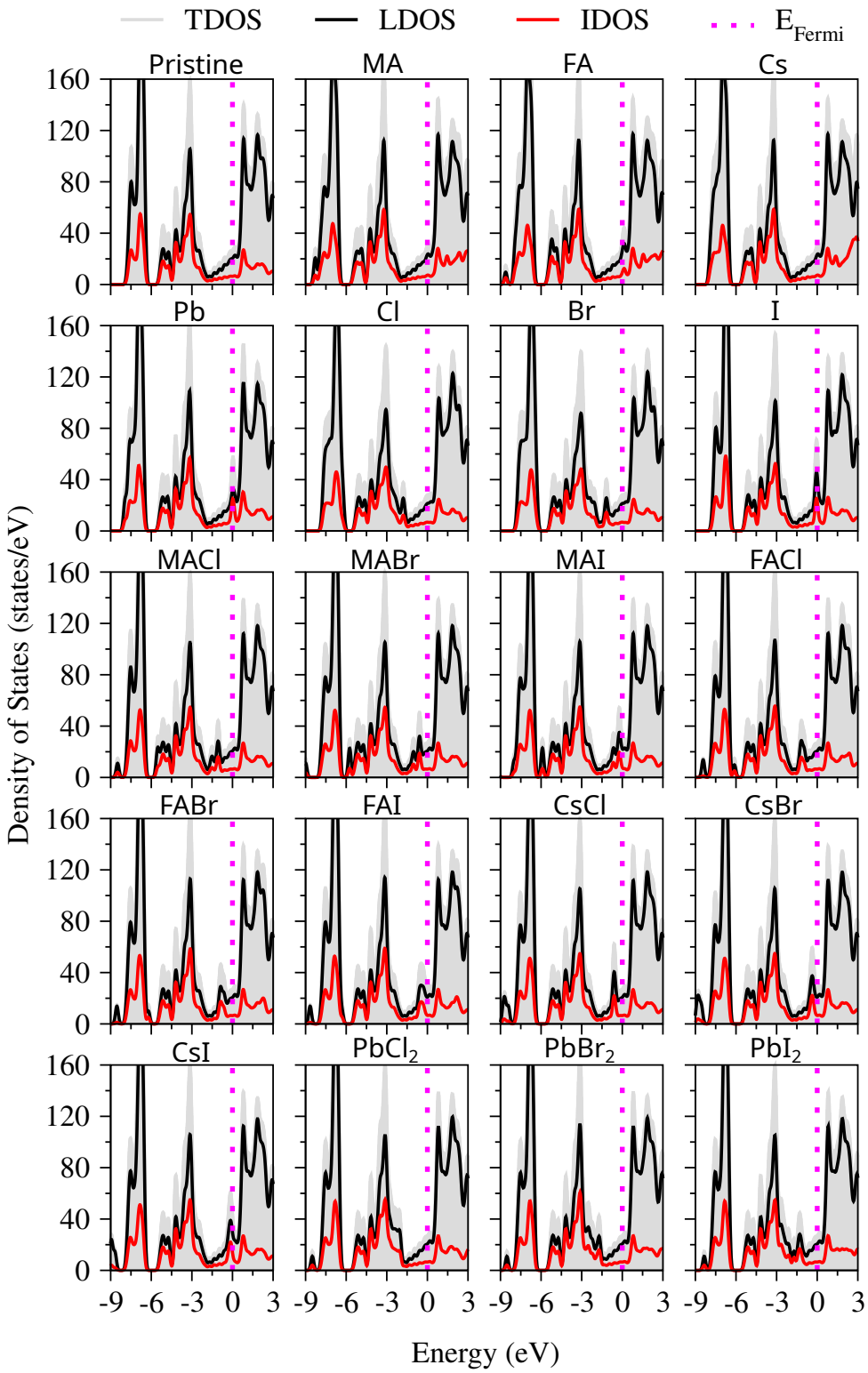

Figure S-8. Total DOS (TDOS), Local DOS (LDOS), and Interstitial DOS (IDOS) as a function of energy for the lowest energy configurations of all optimized structures (i.e., the configurations in bold in Table S-14), along with the pristine structure for reference. The substrate is $Ti_3C_2F_2$ MXene, with each plot explicitly corresponding to a specific system adsorbate/substrate.

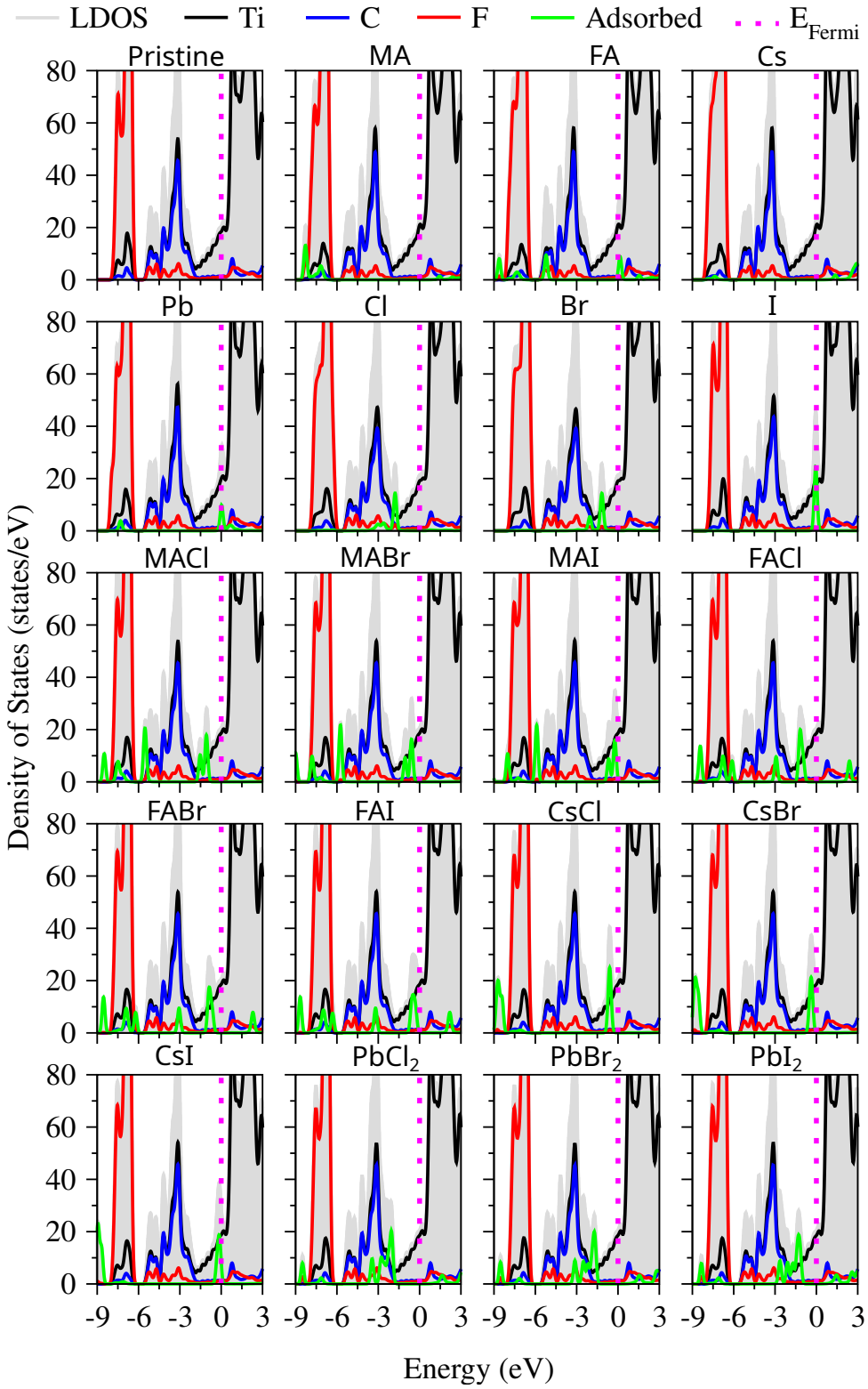

Figure S-9. Local DOS (LDOS) as a function of energy for the lowest energy configurations of all optimized structures (i.e., the configurations in bold in Table S-14), along with the pristine structure for reference. Additionally, we decompose the LDOS into contributions from the atomic species of the $Ti_3C_2F_2$ MXene substrate (Ti, C, and F), with the adsorbate contribution (system adsorbate/substrate) shown exclusively by the green curve.

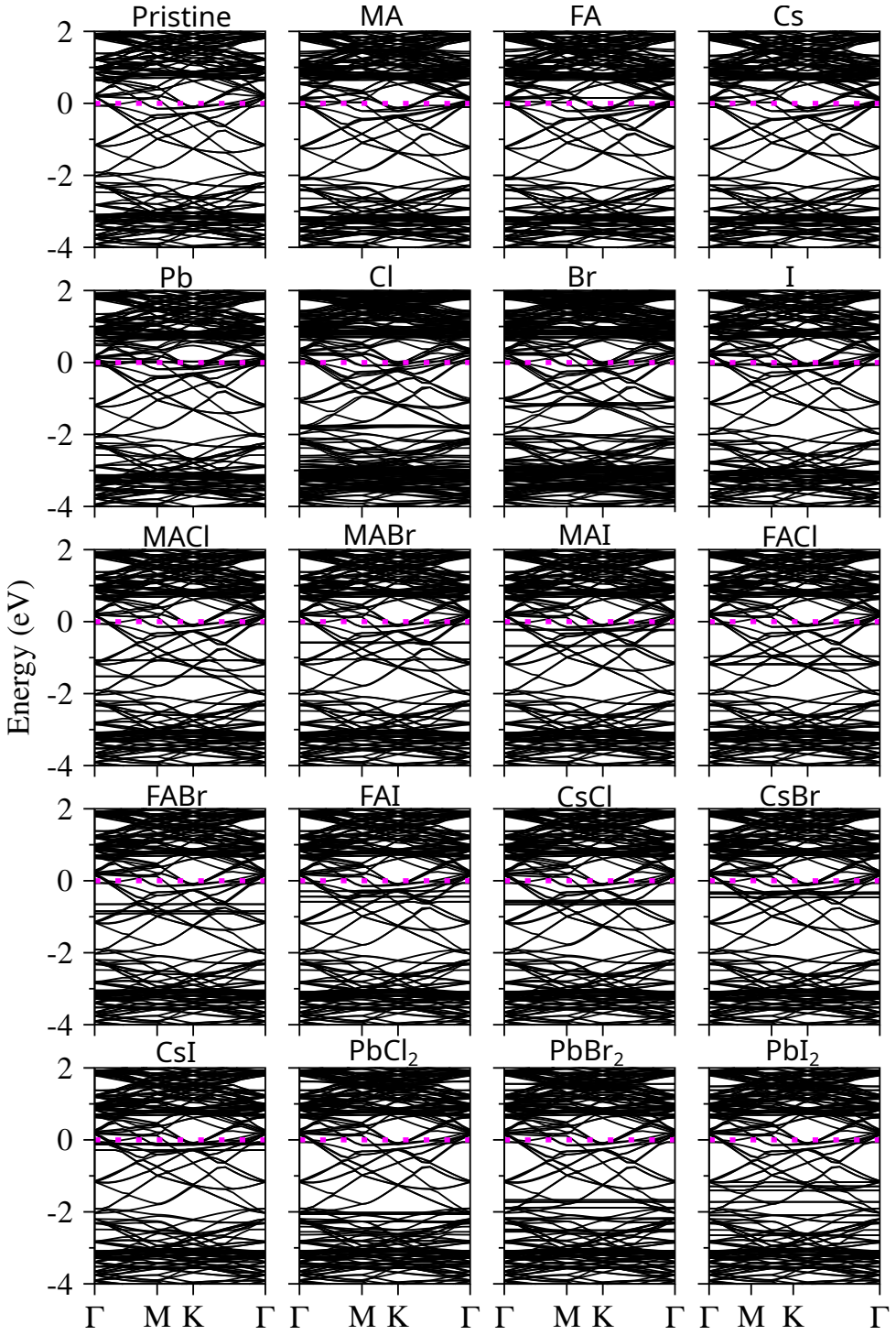

Figure S-10. Band structures, along the high-symmetry path of the Brillouin zone, calculated using the Perdew-Burke-Ernzerhof (PBE) functional, for the lowest energy configurations of all optimized structures (i.e., the configurations in bold in Table S-14), along with the pristine structure for reference.

Table S-18. Bader charge analysis for different adsorbed species on the pristine surface. The table presents the average charge distribution among Ti, C, and F atoms, along with the contribution from the adsorbed fragments. The total charge remains conserved, highlighting the charge transfer between the adsorbate and the substrate. All values are given in units of elementary charge (e). Only the lowest energy configurations (i.e., the configurations in bold in Table S-14) are shown.

Type	Formula	Ti	C	F	Fragment	Total
Pristine	-	493.03	186.72	248.25	-	928.00
A^+	MA^+	494.04	186.92	248.84	28.20	958.00
	FA^+	494.03	186.92	248.87	36.18	966.00
	Cs^+	493.99	186.97	248.92	16.11	946.00
B^{2+}	Pb^{2+}	493.51	186.83	248.63	31.04	960.00
X^-	Cl^-	492.29	186.67	247.96	15.08	942.00
	Br^-	492.34	186.65	248.03	14.99	942.00
	I^-	492.48	186.64	248.11	14.77	942.00
AX	MACl	492.97	186.75	248.34	43.94	972.00
	MABr	492.98	186.76	248.37	43.90	972.00
	MAI	493.00	186.76	248.40	43.84	972.00
	FACl	492.99	186.74	248.38	51.89	980.00
	FABr	493.00	186.74	248.41	51.86	980.00
	FAI	493.01	186.75	248.43	51.81	980.00
	CsCl	493.01	186.73	248.40	31.86	960.00
	CsBr	493.03	186.74	248.42	31.82	960.00
	CsI	493.05	186.74	248.45	31.76	960.00
BX_2	$PbCl_2$	493.00	186.72	248.33	59.96	988.00
	$PbBr_2$	493.00	186.72	248.36	59.93	988.00
	PbI_2	492.97	186.75	248.40	59.88	988.00

Table S-19. Effective Bader charge (Q_{eff}) analysis for different atomic species and compounds. The table presents the total Bader charge (Q), the valence charge (Z_{val}), and the effective charge ($Q_{eff} = Z_{val} - Q$). All values are given in units of elementary charge (e). Only the lowest energy configurations (i.e., the configurations in bold in Table S-14) are shown.

Type	Formula	Q	Z_{val}	Q_{eff}
A^+	MA^+	14.10	15.00	0.90
	FA^+	18.09	19.00	0.91
	Cs^+	8.06	9.00	0.94
B^{2+}	Pb^{2+}	15.52	16.00	0.48
X^-	Cl^-	7.54	7.00	−0.54
	Br^-	7.50	7.00	−0.50
	I^-	7.39	7.00	−0.39
AX	MACl	21.97	22.00	0.03
	MABr	21.95	22.00	0.05
	MAI	21.92	22.00	0.08
	FACl	25.95	26.00	0.05
	FABr	25.93	26.00	0.07
	FAI	25.91	26.00	0.09
	CsCl	15.93	16.00	0.07
	CsBr	15.91	16.00	0.09
	CsI	15.88	16.00	0.12
BX_2	$PbCl_2$	29.98	30.00	0.02
	$PbBr_2$	29.97	30.00	0.03
	PbI_2	29.94	30.00	0.06

Table S-20. Description of Thermodynamic Properties in the Gas Phase

Formula	T	G_{ad}^{gas}	ZPE^{gas}	$\int C_p dT^{gas}$	$-TS^{gas}$
MA^+	0.15	1.9381	1.9378	0.0000	0.0003
	298.15	1.6338	1.9378	0.1652	−0.4692
FA^+	0.15	0.00	0.00	0.00	0.00
	298.15	0.00	0.00	0.00	0.00
Cs^+	0.15	0.00	0.00	0.00	0.00
	298.15	0.00	0.00	0.00	0.00
Pb^{2+}	0.15	0.00	0.00	0.00	0.00
	298.15	0.00	0.00	0.00	0.00
Cl^-	0.15	0.00	0.00	0.00	0.00
	298.15	0.00	0.00	0.00	0.00
Br^-	0.15	0.00	0.00	0.00	0.00
	298.15	0.00	0.00	0.00	0.00
I^-	0.15	0.00	0.00	0.00	0.00
	298.15	0.00	0.00	0.00	0.00
MACl	0.15	0.00	0.00	0.00	0.00
	298.15	0.00	0.00	0.00	0.00
MABr	0.15	0.00	0.00	0.00	0.00
	298.15	0.00	0.00	0.00	0.00
MAI	0.15	0.00	0.00	0.00	0.00
	298.15	0.00	0.00	0.00	0.00
FACl	0.15	0.00	0.00	0.00	0.00
	298.15	0.00	0.00	0.00	0.00
FABr	0.15	0.00	0.00	0.00	0.00
	298.15	0.00	0.00	0.00	0.00
FAI	0.15	0.00	0.00	0.00	0.00
	298.15	0.00	0.00	0.00	0.00
CsCl	0.15	0.00	0.00	0.00	0.00
	298.15	0.00	0.00	0.00	0.00
CsBr	0.15	0.00	0.00	0.00	0.00
	298.15	0.00	0.00	0.00	0.00
CsI	0.15	0.00	0.00	0.00	0.00
	298.15	0.00	0.00	0.00	0.00
$PbCl_2$	0.15	0.00	0.00	0.00	0.00
	298.15	0.00	0.00	0.00	0.00
$PbBr_2$	0.15	0.00	0.00	0.00	0.00
	298.15	0.00	0.00	0.00	0.00
PbI_2	0.15	0.00	0.00	0.00	0.00
	298.15	0.00	0.00	0.00	0.00

References

1 Li, C.; Lu, X.; Ding, W.; Feng, L.; Gao, Y.; Guo, Z. Formability of ABX_3 (X = F, Cl, Br, I) halide perovskites. *Acta Crystallogr. B* **2008**, *64*, 702–707, DOI: 10.1107/S0108768108032734.

2 Green, M. A.; Ho-Baillie, A.; Snaith, H. J. The emergence of perovskite solar cells. *Nat. Photonics* **2014**, *8*, 506–514, DOI: 10.1038/nphoton.2014.134.

3 Naguib, M.; Mochalin, V. N.; Barsoum, M. W.; Gogotsi, Y. 25th Anniversary Article: MXenes: A New Family of Two-Dimensional Materials. *Adv. Mater.* **2014**, *26*, 992–1005, DOI: 10.1002/adma.201304138.

4 Gogotsi, Y.; Anasori, B. The Rise of MXenes. *ACS Nano* **2019**, *13*, 8491–8494, DOI: 10.1021/acsnano.9b06394.

5 Galagan, Y. Perovskite solar cells from lab to fab: the main challenges to access the market. *Oxford Open Mater. Sci.* **2021**, *1*, itaa007, DOI: 10.1093/oxfmat/itaa007.

6 Wu, Z.; Cohen, R. E. More accurate generalized gradient approximation for solids. *Phys. Rev. B* **2006**, *73*, 235116, DOI: 10.1103/PhysRevB.73.235116.

7 Naguib, M.; Kurtoglu, M.; Presser, V.; Lu, J.; Niu, J.; Heon, M.; Hultman, L.; Gogotsi, Y.; Barsoum, M. W. Two-Dimensional Nanocrystals Produced by Exfoliation of Ti_3AlC_2. *Adv. Mater.* **2011**, *23*, 4248–4253, DOI: 10.1002/adma.201102306.

8 Khazaei, M.; Arai, M.; Sasaki, T.; Chung, C.-Y.; Venkataramanan, N. S.; Estili, M.; Sakka, Y.; Kawazoe, Y. Novel Electronic and Magnetic Properties of Two-Dimensional Transition Metal Carbides and Nitrides. *Adv. Funct. Mater.* **2013**, *23*, 2185–2192, DOI: 10.1002/adfm.201202502.

9 Xie, Y.; Kent, P. R. C. Hybrid density functional study of structural and electronic properties of functionalized $Ti_{n+1}X_n$ (X = C, N) monolayers. *Phys. Rev. B* **2013**, *87*, 235441, DOI: 10.1103/PhysRevB.87.235441.

10 Heyd, J.; Scuseria, G. E.; Ernzerhof, M. Hybrid Functionals Based on a Screened Coulomb Potential. *J. Chem. Phys.* **2003**, *118*, 8207–8215, DOI: 10.1063/1.1564060.

11 Hu, T.; Wang, J.; Zhang, H.; Li, Z.; Hu, M.; Wang, X. Vibrational properties of Ti_3C_2 and $Ti_3C_2T_2$ (T = O, F, OH) monosheets by first-principles calculations: a comparative study. *Phys. Chem. Chem. Phys.* **2015**, *17*, 9997–10003, DOI: 10.1039/C4CP05666C.

12 Kong, L.; Liang, X.; Deng, X.; Guo, C.; Wu, C.-M. L. Adsorption of SF_6 Decomposed Species on $Ti_3C_2O_2$ and $Ti_3C_2F_2$ with Point Defects by DFT Study. *Adv. Theory Simul.* **2021**, *4*, 2100074, DOI: 10.1002/adts.202100074.

13 Ibaceta-Jaña, J.; Muydinov, R.; Rosado, P.; Mirhosseini, H.; Chugh, M.; Nazarenko, O.; Dirin, D. N.; Heinrich, D.; Wagner, M. R.; Kühne, T. D.; Szyszka, B.; Kovalenko, M. V.; Hoffmann, A. Vibrational dynamics in lead halide hybrid perovskites investigated by Raman spectroscopy. *Phys. Chem. Chem. Phys.* **2020**, *22*, 5604–5614, DOI: 10.1039/C9CP06568G.